This article has been accepted for publication in a future issue of this journal, but has not been fully edited. Content may change prior to final publication. Citation information: DOI 10.1109/TMI.2014.2375065, IEEE Transactions on Medical Imaging

Magnetic Particle Imaging with Tailored Iron Oxide Nanoparticle Tracers

R. Matthew Ferguson, Amit P. Khandhar, Scott J. Kemp, Hamed Arami, Emine U. Saritas, Laura R. Croft, Justin Konkle, Patrick W. Goodwill, Aleksi Halkola, Jürgen Rahmer, Jörn Borgert, Steven M. Conolly, and Kannan M. Krishnan*

***Abstract*— Magnetic Particle Imaging (MPI) shows promise for medical imaging, particularly in angiography of patients with chronic kidney disease. As the first biomedical imaging technique that truly depends on nanoscale materials properties, MPI requires highly optimized magnetic nanoparticle tracers to generate quality images. Until now, researchers have relied on tracers optimized for MRI T2*-weighted imaging that are sub-optimal for MPI. Here, we describe new tracers tailored to MPI's unique physics, synthesized using an organic-phase process and functionalized to ensure biocompatibility and adequate *in vivo* circulation time. Tailored tracers showed up to 3x greater SNR and better spatial resolution than existing commercial tracers in MPI images of phantoms.**

***Index Terms*—Magnetic Particle Imaging, biomedical imaging, superparamagnetic iron oxides**

I. Introduction

MAGNETIC particle imaging (MPI) shows great promise in many clinical applications ranging from angiography to cancer theranostics and molecular imaging [1]-[3], as future clinical MPI scanners will potentially provide real-time, 3D visualization of magnetic nanoparticles (MNPs) within a patient. MPI scanners utilize an oscillating magnetic field (the drive field) to generate a signal by exciting the non-linear magnetization of MNP tracers. A superimposed magnetic gradient field (the selection field) localizes the signal, allowing image formation. MPI is capable of extremely fast imaging [4] with outstanding contrast, sensitivity, and depth penetration [1], [2], [4], [5]. MPI will use safe iron oxide MNP tracers to offer important advances for clinical imaging and patient safety. Iodine and gadolinium tracers used in X-ray imaging and magnetic resonance imaging, respectively, are hazardous for patients with chronic kidney disease (CKD) [6], [7]. Today, 35% of Americans over 60 have CKD [8]. In contrast, MPI uses MNPs that are safe for CKD patients [9], [10] and magnetic fields instead of ionizing radiation. Furthermore, MNPs between 15 and 100 nm hydrodynamic diameter avoid renal clearance when coated with suitable surface coatings [11] and are small enough to promote longer circulation time that can be exploited for angiography or imaging of macrophages and inflammation [12]. MNPs are also suitable for *in vivo* applications in cell tracking using MPI [13], [14].

MPI offers advantages over other medical imaging modalities: the MPI signal is generated solely by MNPs, with zero background signal generated by diamagnetic tissue, resulting in unprecedented vascular contrast [2], [4], [15]. Estimates of ~20 nM sensitivity and sub-mm resolution are predicted by MPI theory [1], [5], [16], [17]. MPI also shows promise for quantitative imaging, since it is intrinsically-linear [1] at particle concentrations used in vivo, with signal that scales with the amount of MNPs per voxel. Linearity has been demonstrated mathematically and experimentally [18], but it requires non-interacting particle systems and careful avoidance of non-linearities in the signal chain or imprudent filtering in signal processing and image reconstruction. However, MPI's full potential could not yet be demonstrated in experiments, because we have lacked MNPs that are tailored to the unique MPI physics, with rapid magnetic relaxation under alternating fields in a biological environment. MPI is exquisitely sensitive to MNP size and distribution [16], [19], [20], but available iron oxide nanoparticles, such as *Resovist*® (ferucarbotran, Bayer Schering Pharma, Berlin, Germany), were developed for MRI T2* contrast and feature sub-optimal magnetic properties because they contain magnetic cores that are small (<10 nm diameter) and polydisperse.

Here we describe MNP tracers specifically tailored to MPI

This work was supported by NIH grants 1R01EB013689-01/NIBIB and 2R42EB013520-02A1, NSF grant IIP-1215556, a UW/CGF commercialization grant and a Commercialization Fellowship (RMF). AH, JR, and JB acknowledge funding by the German Federal Ministry of Education and Research (BMBF grants FKZ 13N9079 and 13N11086). ES, LG, PG, and SC also acknowledge funding from a CIRM Tools and Technology Grant (RT2-01893) and a UC Discovery Grant. *Asterisk indicates corresponding author.*

R. M. Ferguson, A. P. Khandhar, and S. J. Kemp are with LodeSpin Labs, PO Box 95632, Seattle, WA 98145

H. Arami, and K. M. Krishnan (e-mail: kannanmk@uw.edu) are with the Department of Materials Science, Roberts Hall, University of Washington, Seattle, WA 98195 USA.

E. U. Saritas, L. R. Croft, J. Konkle, P. W. Goodwill and S. M. Conolly are with the Department of Bioengineering, University of California, Berkeley, CA 94720 USA. S. M. Conolly is also with the EECS, Berkeley, CA 94720 USA.

A. Halkola is with Institute of Medical Engineering, University of Lübeck, Lübeck, Germany.

J. Rahmer and J. Borgert are with Philips Technologie, GmbH, Research Laboratories, Hamburg, Germany

This article has been accepted for publication in a future issue of this journal, but has not been fully edited. Content may change prior to final publication. Citation information: DOI 10.1109/TMI.2014.2375065, IEEE Transactions on Medical Imaging

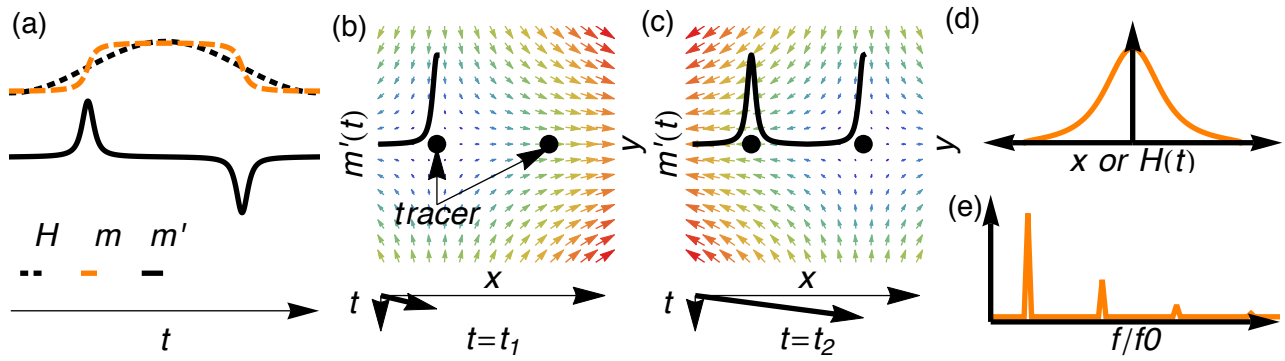

Figure 1. Schematic illustration of MPI detection and size-dependent tracer magnetic properties. (a) The characteristic nonlinear magnetic response ($m(t)$ and its derivative $m'(t)$) of superparamagnetic nanoparticles to an applied field, *H*. (b, c) As the field free point sweeps over a location that contains MNPs, $m'(t)$ changes rapidly, generating a signal that reveals the MNP location. In (b) and (c), $m'(t)$ (black curve) is shown for all time $t < t_n$, while the FFP, which is moving from left to right with time, is represented at $t = t_n$, where n = 1 or 2. MPS signals: (d) $m'(H)$, the tracer response, determines the point spread function (PSF, $m'(Gx)$) when the system field gradient, *G*, is known; (e) the harmonic spectrum, $\mathcal{F}(m')$, is used to evaluate tracers for *System Matrix* MPI reconstruction.

and demonstrate dramatic improvements in MPI sensitivity and spatial resolution, relative to the current commercial standard, *Resovist*®. Development of such superior tracers will accelerate MPI's clinical translation.

II. MPI Signal Acquisition and Image Reconstruction

MPI exploits the nonlinear magnetization (Figure 1(a)) of superparamagnetic nanoparticles to generate a localized signal during imaging. A modulating magnetic field, $H(t)$, (typically ~25 kHz, ~20 mT/μ_0 amplitude) excites MNPs and the nonlinear response of their moment, $m(H)$, induces in a receive coil a signal voltage proportional to $m'(H)$ (Figure 1(a)). An additional gradient, called the selection field, is applied to localize the received signal. The selection field features a field free point (FFP) surrounded by a gradient with sufficient strength to saturate the magnetization of MNPs located outside the FFP. (Typical gradients are ~1-7 T/μ_0/m). Images are formed by scanning the FFP through the sample and recording the MPI signal (Figure 1(b, c)). Scanners that use field free line selection fields have also been designed [21], [22] and demonstrated [23], [24].

MPI image reconstruction is an area of ongoing research and several approaches have been demonstrated (see Grüttner, et al. for a detailed review and comparison of published approaches to MPI reconstruction [25]). In the original *System Matrix* reconstruction [1], [26], images are formed by recording the Fourier transform of the received signal and solving the inverse imaging problem using a predetermined matrix (called the System Function) that contains the system response to a point source measured at each point within the imaging volume [26], [27]. The System Function can be measured [1], which is most accurate but time-consuming, or it can be simulated with models to reduce the acquisition time [28], at the expense of some accuracy. In *x-space* MPI reconstruction [17], [29] the instantaneous MPI signal is assigned to the current FFP location after compensating for the FFP velocity. The MPI image can be expressed as a convolution between the MNP distribution and the point spread function (PSF), $h(x) = m'(Gx)$, where G is the gradient strength [T/μ_0/m]. Lu, et al. showed that the MPI image is linear and shift invariant using this approach [18].

Whether using *System Matrix* or *x-space* reconstruction, MPI physics is governed by the tracer response, defined as the derivative of tracer magnetization, $m'(H)$ [m^3], and the excitation field slew rate, Gx_s' [T/μ_0/s], where x_s' is the FFP velocity [m/s]. The tracer response is recognized to be a crucial determinant of SNR and spatial resolution. As we demonstrate here, image quality can be dramatically improved in both reconstruction approaches by tailoring the tracer response.

MPI scanners being currently scarce, MNP performance is commonly measured using a Magnetic Particle Spectrometer (MPS) [30] or an MPI *x-space* relaxometer [15]. These scanners lack a gradient field, but directly measure the tracer response, $m'(H)$ (Figure 1(d)), under typical conditions (the spectrometer displays $\mathcal{F}(m')$, see Figure 1(e)). A broader spectrum measured by the spectrometer is equivalent to a narrower tracer response measured by the relaxometer and indicates superior spatial resolution; intensity per unit iron indicates the concentration-independent tracer contribution to SNR.

III. Materials and Methods

A. Synthesis & characterization of iron oxide nanoparticle tracers

Three iron oxide MNP tracer samples, UW-1, UW-2, and LS-1 were used in phantom experiments reported here. Physical properties of the samples are listed in Table 1. Tracers were synthesized according to protocols described in previous work [31]. Synthesis protocols were based on thermolysis of iron (III) oleate with excess oleic acid in 1-octadecene. After synthesis, oleic acid coated MNPs were transferred from organic to aqueous phase using a PEG-ylated amphiphilic polymer [poly(maleic anhydride-alt-1 octadecene)-poly(ethylene glycol); PEG M_w ~ 5,000 Da (UW-1, UW-2) or 20,000 Da (LS-1)]. All three samples showed

This article has been accepted for publication in a future issue of this journal, but has not been fully edited. Content may change prior to final publication. Citation information: DOI 10.1109/TMI.2014.2375065, IEEE Transactions on Medical Imaging

comparable magnetic behavior measured by MPS and vibrating sample magnetometer (VSM); the thicker polymer coating of sample LS-1 was designed to prolong blood circulation time for ongoing animal studies unrelated to this work. MNP magnetic size was determined by bright field TEM imaging (FEI, Hillsboro, OR) and by fitting a Langevin function to room-temperature magnetization curves (VSM, Lakeshore, Westerville, OH) to determine the median magnetic core diameter (d_0) and geometric standard deviation ($\exp(\sigma)$), assuming the particle sizes satisfied a log normal distribution of the form

$$g(d_c) = \frac{1}{\sigma d_c \sqrt{2\pi}} \exp - \frac{\left[\ln\left(\frac{d_c}{d_0}\right)\right]^2}{2\sigma^2}, \quad (1)$$

where d_c is the magnetic core diameter [19]. The number-weighted diameter distribution was determined to enable direct comparison with TEM. For fitting *M(H)* data, the saturation magnetization, M_s, was determined from measured iron concentration; average M_s was 2.8×10^5 A/m, (UW-1: 1.5×10^5; UW-2: 3.7×10^5; LS-1: 3.3×10^5 A/m), similar to the measured M_s of *Resovist*® (3.0×10^5). Sample iron concentration was measured by inductively coupled plasma - optical emission spectrophotometer (ICP) (Perkin Elmer, Waltham, MA). Z-average hydrodynamic diameter, d_H, of aqueous-phase MNPs was determined by Dynamic Light Scattering (DLS) (Zetasizer, Malvern Instruments, Malvern, UK).

Table 1. Core and hydrodynamic diameters of samples used for phantom imaging.

	d_0 [nm] (σ)		d_H [nm] (PDI)
	TEM	VSM	
UW-1	27 (0.22)	34 (0.07)	54 (0.14)
UW-2	27 (0.17)	26 (0.05)	47 (0.16)
LS-1	26 (0.06)	28 (0.06)	72 (0.12)

B. MPS analysis

Magnetic Particle Spectrometry and *x-space* relaxometry were used to evaluate MPI performance of candidate tracer formulations. All measurements were performed at UW at f = 25.25 kHz, H_{max} = 16 mT/μ_0, using the combined spectrometer/*x-space* relaxometer described in previous work [20].

The MPS applies a time-varying magnetic field

$$H(t) = H_0 \sin(\omega t),$$

where H_0 is the peak excitation amplitude and ω the angular frequency ($2\pi f_0$), to magnetize the tracer and measure a signal voltage, *V(t)* [17], [20], [32]

$$V(t) = -\mu_0 \cdot S \cdot m'(t) = -\mu_0 \cdot S \cdot m'(H(t)) \cdot H'(t)$$

where μ_0 is the vacuum permeability [$4\pi\times10^{-7}$ Vs/Am], S is the coil sensitivity [1/m], and *m'(t)* [A/m/s] is the derivative of the tracer magnetic moment, *m(t)* [A/m]. Re-arranging yields

$$m'(H) = \frac{-1}{\mu_0 S \omega H_0} \frac{V(t)}{\cos(\omega t)}, \quad (2)$$

which is visualized as a parametric plot {H, dm/dH} since the field, *H(t)*, is known for all times t. We note this approach encodes the effects of particle dynamics into *m'(H)*.

C. Fast system matrix MPI imaging

Imaging System. One set of phantoms was imaged using System Matrix reconstruction and the Pre-Clinical Demonstrator (PCD) scanner at Philips Research laboratories in Hamburg [33]. The PCD applies orthogonal drive fields at frequencies centered on 25 kHz, with field amplitude of 16 mT/μ_0, to generate a Lissajous scan trajectory. Selection field gradients are 1.25 T/m/μ_0 in the x and y directions, which define the plane of the phantom, and 2.5 T/m/μ_0 in the z direction.

Phantoms and Measurements. Phantoms were constructed from clear plastic tubing with an inner diameter of 1.5 mm. The letter P was made of one piece, whereas the letter H was made of three pieces. The phantom measured 48 mm by 32 mm. Two phantoms were created and filled with *Resovist*®, and UW-2, respectively. *Resovist*® was diluted with 0.9% NaCl solution to the same iron concentration (0.95 gFe/L) as UW-2 for the phantom measurement. Since the phantoms were larger than the field-of-view (FOV), focus fields were used to shift the FOV to six patches around the object [33], [34], which were then combined to form a single image. At each focus station the signal from one Lissajous period was measured. It was necessary to wait for four Lissajous periods between stations before a new acquisition could take place, in order to wait for the focus fields to settle. With appropriate compensation strategies and continuous focus field variation this dead time can be substantially reduced [35]. The total measurement time is 560 ms, of which 129 ms are phantom measurements and 431 ms waiting between stations.

System Function. For *system matrix* reconstruction it is necessary to obtain a separate system function (SF) for each tracer. A grid of 30 x 30 x 20 positions was measured using focus fields [36]. The SF covers a volume of 36 x 36 x 20 mm³. The sample used for the calibration was a cylinder with a diameter of 1 mm and length of 2 mm. At each SF position the signal from 20 Lissajous periods was averaged, to ensure noise in the SF was significantly lower compared to the phantom measurements. As the same SF was used for all six reconstructed stations, slight distortions occur at the edges of the image.

D. x-space MPI imaging

This article has been accepted for publication in a future issue of this journal, but has not been fully edited. Content may change prior to final publication. Citation information: DOI 10.1109/TMI.2014.2375065, IEEE Transactions on Medical Imaging

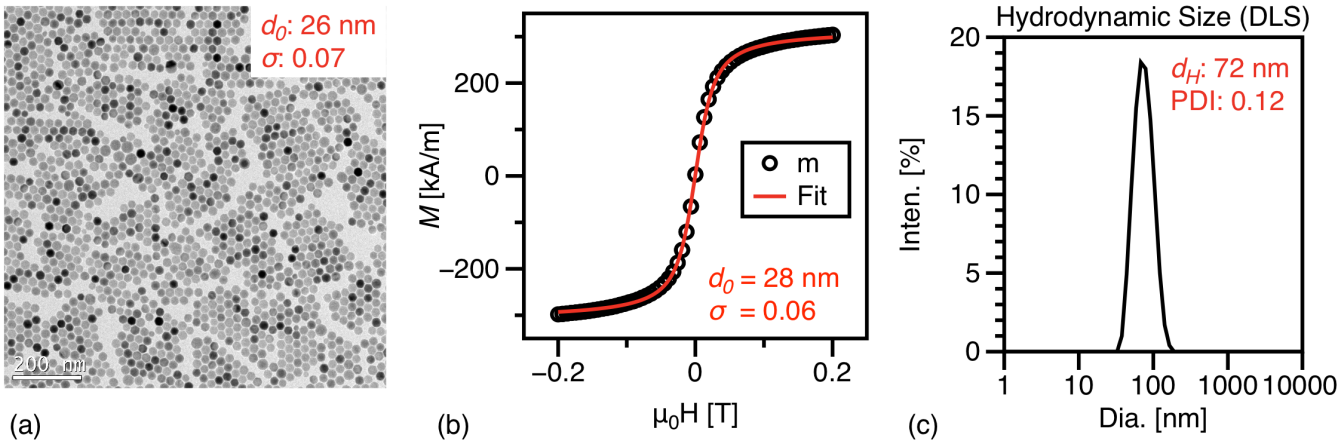

Figure 2. MNP size characterization of LS-1. (a) Bright field TEM image of magnetite particles. In this example, median crystal diameter was determined to be 26 nm from statistical analysis of TEM images (6000 particle counts), assuming a log-normal distribution. (b) Median magnetic core diameter was determined to be 28 nm by fitting *M(H)* data to the Langevin function and assuming a log-normal size distribution. (c) Hydrodynamic diameter (~72 nm, Z-average) was measured using dynamic light scattering.

Imaging System. A second set of phantoms was imaged in the 3D MPI scanner [37],[38] at the Berkeley Imaging Systems Labs, University of California, Berkeley. This scanner creates an FFP with a magnetic field gradient of 7 T/m/μ_0 in the x direction and 3.5 T/m/μ_0 in the y and z directions. The drive field coil scanned the imaging FOV at 23.2 kHz, with field amplitude 25 mT/μ_0. The system uses a raster scan trajectory [38].

UW Phantom Imaging and Image Reconstruction. The letters "UW" were laser-cut in 1.5 mm wide, 1.5 mm deep channels into clear acrylic. These channels were filled with 550 µL of 0.29 g(Fe)/L diluted tracer. Two such phantoms were created, one filled with *Resovist*® and the other with UW-1. The dimensions of the resulting acrylic phantoms were 3.8 x 0.6 x 9.2 cm^3. These phantoms were imaged separately on the Berkeley MPI scanner with an imaging FOV of 4.5 x 4.5 x 14 cm^3. Total imaging time was 3 min 20 s for each phantom. The images were reconstructed via *x-space* MPI reconstruction [17], [29]. Accordingly, the received MPI signal was compensated by the instantaneous velocity of the FFP, and assigned to the instantaneous spatial-position of the FFP. Note that because the FFP trajectory is defined in the pulse sequence, both the velocity and the position of the FFP are known at all times. This simple image reconstruction technique does not require any *a priori* knowledge about the MNP tracer or its magnetization response characteristics. The resulting MPI image is referred to as the "native" MPI image. For the "UW" phantom imaging experiment, mild deconvolution was performed primarily to reduce background signal "haze." Specifically, we applied Wiener deconvolution (Matlab R2014a, The MathWorks, Inc., Natick, MA) with an assumed noise level that minimally changed the measured FWHM. The inputs to the Wiener deconvolution are the native image and a theoretical PSF generated using a nanoparticle diameter and standard deviation that best matched the measured PSF [29]. Measured PSFs were obtained by imaging, using the same imaging conditions as the UW phantom, point sources constructed by filling a short length of 0.8mm I.D. tubing with 3 µL of tracer.

Resolution phantom. Resolution phantoms were constructed from microbore PTFE tubing (0.56 mm I.D., 1.07 mm O.D.; Cole-Parmer 06417-21). Point sources were approximated by injecting 0.5 µL of sample into the tubing to create a liquid column with 0.56 mm diameter and 2.1 mm height. Resovist® was used undiluted (28 gFe/L) to ensure sufficient SNR, while the LS-1 sample concentration was 1.9 gFe/L. Point sources were arranged in a linear array with increasing number of empty spacer tubes between the sample points. Edge to edge spacings between the liquid cylinders were 3.8, 2.7, 1.6, and 0.6 mm. Phantoms were imaged in the Berkeley 3D MPI scanner. Imaging time was 6 minutes per phantom and the FOV was 6 x 3 x 3 cm^3. The drive field amplitude was 20 mT/μ_0 at 23.2 kHz.

IV. Results and Discussion

A. Magnetic Particle Spectroscopy

Measurements of MNP core diameter by TEM typically showed good agreement with the magnetic size determined by fitting to *M(H)*. The diameter measured by TEM (Fig 2(a)) was typically slightly smaller than the volume-weighted magnetic diameter (Fig 2(b)), but slightly larger than the number-weighted magnetic diameter (table 1). Mean hydrodynamic diameter (intensity-weighted) of the tracers, after coating with PMAO-PEG, was about 45 or 75 nm (Fig 2(c)), depending on the chosen polymer.

Equilibrium magnetization measurements of selected water-based MNP formulations (Figure 3(a)) showed that *M(H)* curves became increasingly nonlinear with increasing size, as susceptibility increased and saturation field decreased, respectively. MNPs were characterized using our MPS system [20] at f_0 = 25 kHz, H_{max} ~ 16 mT/μ_0. The MPS system was configured to measure the performance metrics for *System Matrix* and *x-space* reconstruction, which are interrelated by a temporal Fourier transform. All metrics improved with increasing diameter and ~25 nm MNPs showed the most optimal response. Harmonic spectra (calculated from

This article has been accepted for publication in a future issue of this journal, but has not been fully edited. Content may change prior to final publication. Citation information: DOI 10.1109/TMI.2014.2375065, IEEE Transactions on Medical Imaging

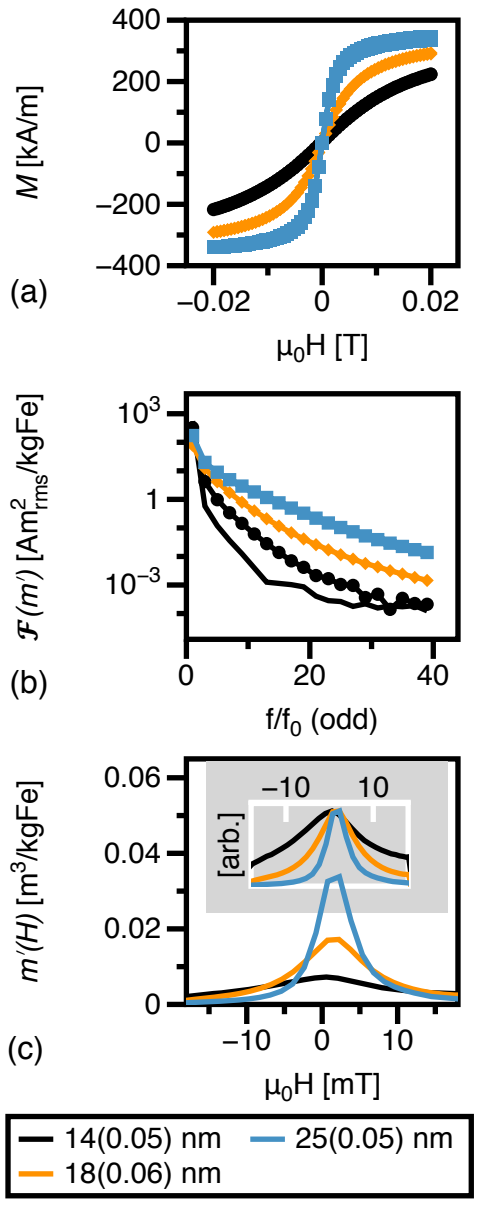

Figure 3. MNP magnetic properties. (a) Measured *M(H)* loops for water-suspended MNPs of the specified median diameter and distribution width, σ. (b) Measured harmonic spectra, showing only odd harmonics. The system noise floor is also shown (solid line). (c) Measured tracer response, scaled by iron content and normalized to 1 for comparison of FWHM (inset). Only scans of increasing *H* are shown in the figure.

$\mathcal{F}(m'(H))$ and tracer responses $(m'(H))$ are shown in Figure 3(b) and Figure 3(c), respectively.

A summary of measurements for selected water-based MNP formulations produced in our labs, as well as commercial references *Resovist*® and *Feridex*™ (ferumoxides), is provided in Figure 4. MPI performance is represented using the tracer response full width at half maximum (FWHM) [mT/μ_0] (Figure 4(a)) and normalized maximum intensity [V/mg(Fe)] (Figure 4(b)). In the figure, spot size is proportional to the relevant performance metric: in Figure 4(a), smaller circles represent narrower FWHM and better performance; in Figure 4(b), larger circles represent greater intensity and better performance. Tracers with the highest normalized signal

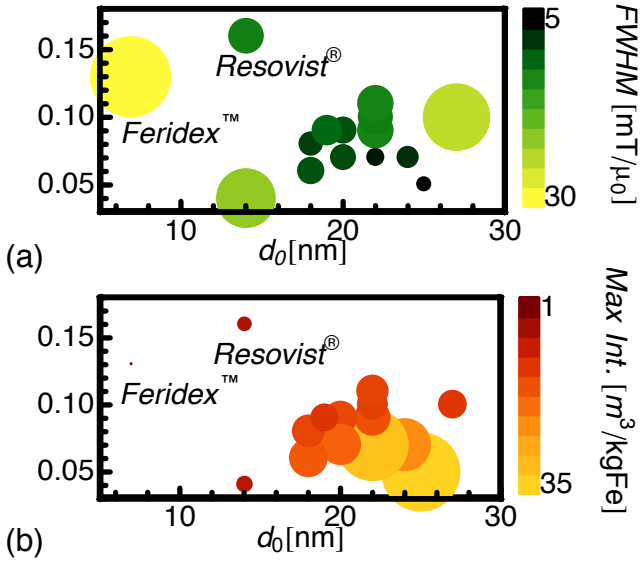

Figure 4. MPI performance is determined largely by MNP core size and size distribution. Here, key performance metrics measured by MPS are presented for different tracer formulations produced during optimization, with both spot size and color proportional to the relevant metric: (a) Spatial resolution (FWHM of tracer response, in mT/μ_0, smallest diameter is best) and (b) Normalized intensity (max intensity of tracer response, in m^3/kgFe, largest diameter is best). According to both metrics, MPI performance improves with increasing core size, provided that size distribution remains narrow.

intensity also featured the best spatial resolution. Furthermore, for similar core sizes, performance improved with decreasing size distribution, σ. We also observed improved performance with increasing magnetic core size when the magnetic core size distribution was narrow (when the unitless log-normal distribution shape parameter, σ, in Eq. 1 was ≤0.1).

To be consistent with other samples in Figure 4, *Resovist*® was fitted to a single log-normal distribution with d_0=14 nm and σ=0.16. However, extensive analysis of *Resovist*® by other authors has shown that it is more accurately modeled using a bi-modal distribution containing 6 and 24 nm diameter fractions. The larger fraction is generally assumed to contribute to the MPI signal [39], [40].

MPS measurements for sample UW-2 and *Resovist*® are provided in Figure 5. Signals were normalized by iron concentration for comparison. Comparing the peak in $m'(H)$, UW-2 showed 6x greater signal intensity than *Resovist*®; the relative difference in harmonic intensities was 3.5x, 12.2x, and 9.8x for the 3rd, 19th, and 39th harmonics, respectively.

B. Phantom Imaging

To demonstrate the capabilities of MPI with tailored tracers, phantoms were constructed and filled with optimized tracers and *Resovist*®, which has been used as the standard in many previous MPI experiments [1], [4]. The "PH" and "UW" phantoms featured 1.5 mm channel widths; the resolution phantom featured 0.56 mm (liquid column diameter) wide point sources.

A photograph of a "PH" phantom is shown in Figure 6(a); reconstructed images, scaled to the same noise level, are shown in Figure 6(b) (UW-2, top and *Resovist*®, bottom). Blue

This article has been accepted for publication in a future issue of this journal, but has not been fully edited. Content may change prior to final publication. Citation information: DOI 10.1109/TMI.2014.2375065, IEEE Transactions on Medical Imaging

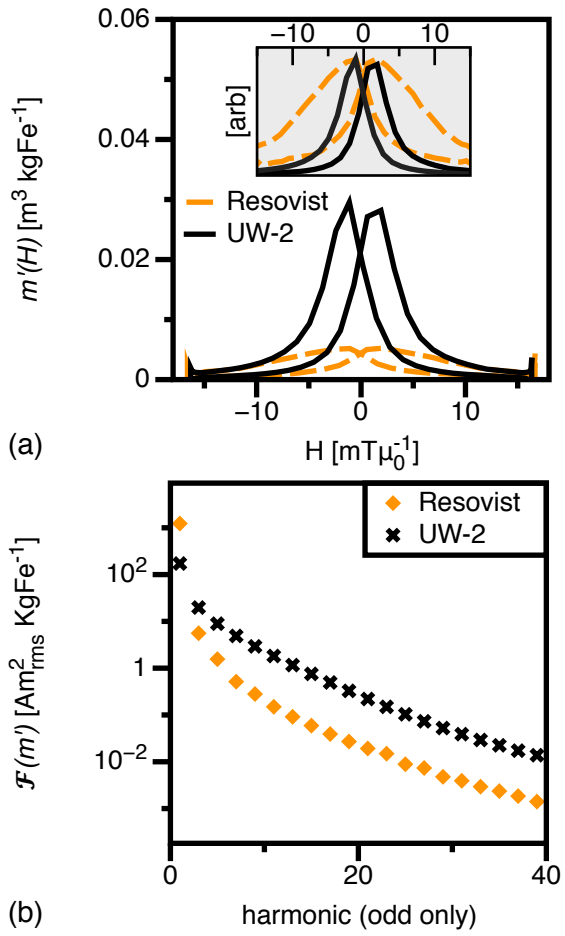

Figure 5. MPS measurements (f_0 = 25kHz, H_{max} = 16 mT/μ_0) of optimized MNPs (UW-2) and *Resovist*®: (a) MNP response, $m'(H)$. Forward (low to high field) and reverse (high to low field) scans are shown. Signal intensity, measured by the $m'(H)$ maximum, of UW-2 was 0.030 m^3/kgFe, 6x greater than *Resovist*® (0.005 m^3/kgFe). Full width at half maximum resolution was 4.7 (mT/μ_0) for UW-2, half that of *Resovist*®. (b) Harmonic spectra of UW-2 and *Resovist*®. UW-2 showed greater harmonic intensity for all harmonics; 3.5x, 12.1x, and 9.8x greater at the 3rd, 19th, 39th harmonics, respectively.

and green lines indicate the sampling positions of the intensity profiles shown in Figure 6(c). Based on the average difference in peak intensity for equivalent positions in Figure 6(c), UW-2 produced 3.3x greater signal intensity than *Resovist*®. The acquisition time for each image was 0.56 s, with 0.43 s of latency.

Additional imaging experiments were performed using a second set of phantoms and the Berkeley 3D MPI scanner and *x-space* reconstruction: images of "UW" phantoms filled with sample UW-1, resolution phantoms filled with sample LS-1, and single point-source phantoms for measuring the system PSF (images not shown). Finer resolution and greater signal intensity were observed with UW-1 in maximum intensity projections of the native (*i.e.*, undeconvolved) MPI images (Figure 7(a)), presented in the *x-z* image plane. In figure 7(b) the same image is shown after mild Weiner deconvolution described previously. A photograph of "UW" phantoms is provided in Figure 7(c), along with mid-line cross sections comparing relative image intensity. Acquisition time for these images was 3 min 20 s for each phantom. Comparing again the average difference in peak intensity at equivalent positions in the intensity profiles of figure 7(c), UW1 showed 1.9x greater intensity than *Resovist*®.

Improved resolution was demonstrated using resolution phantoms filled with LS-1 in the Berkeley 3D MPI scanner. Native maximum-intensity projection images of the resolution phantoms are provided in Figure 8(a,b). A photograph of one of the phantoms is provided in Figure 8(d). Point sources were 0.56 mm wide (liquid column diameter) and separation (edge-edge) between adjacent point sources in the phantom was 0.6, 1.7, 2.7, 3.8 mm, respectively. The points separated by 1.7 mm were well-resolved in the native image of the LS-1 phantom. In the phantom filled with *Resovist*®, only the 3.8 and 2.7 mm pairs were resolved.

C. Discussion

We prepared monodisperse, single-core iron oxide nanoparticles via chemical synthesis in non-polar solvents, followed by coating with a biocompatible PEG-based polymer [31]. To tailor our MPI tracers, we utilized physical models of MNP relaxation in alternating fields [16], [19], [41]. We note that hysteresis was observed in the magnetic behavior (*i.e.*

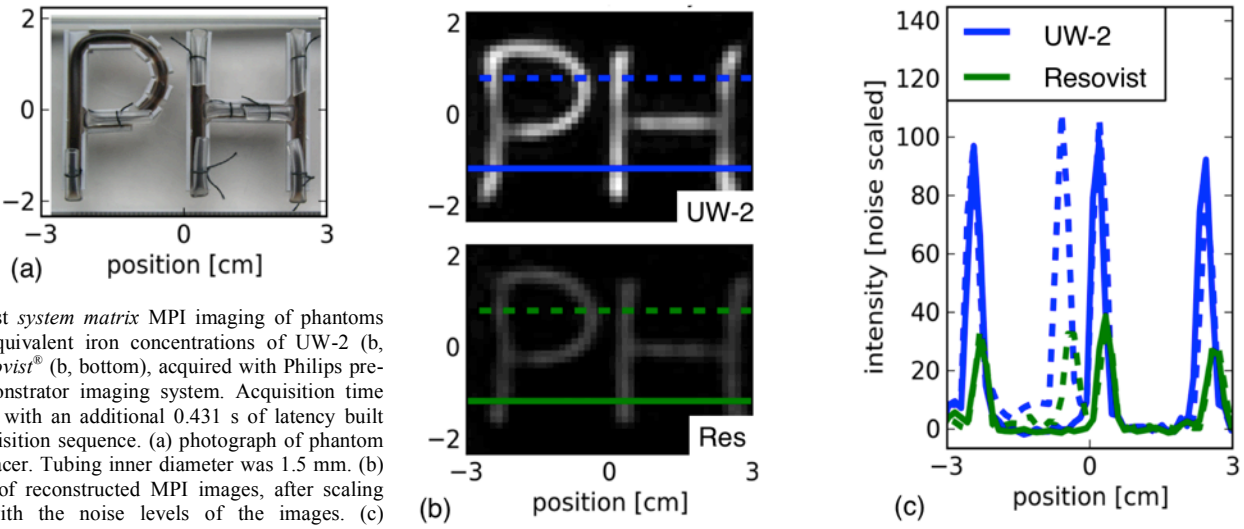

Figure 6. Fast *system matrix* MPI imaging of phantoms containing equivalent iron concentrations of UW-2 (b, top) and *Resovist*® (b, bottom), acquired with Philips pre-clinical demonstrator imaging system. Acquisition time was 0.129 s, with an additional 0.431 s of latency built into the acquisition sequence. (a) photograph of phantom filled with tracer. Tubing inner diameter was 1.5 mm. (b) Comparison of reconstructed MPI images, after scaling intensities with the noise levels of the images. (c) Intensity profiles obtained from phantom images.

This article has been accepted for publication in a future issue of this journal, but has not been fully edited. Content may change prior to final publication. Citation information: DOI 10.1109/TMI.2014.2375065, IEEE Transactions on Medical Imaging

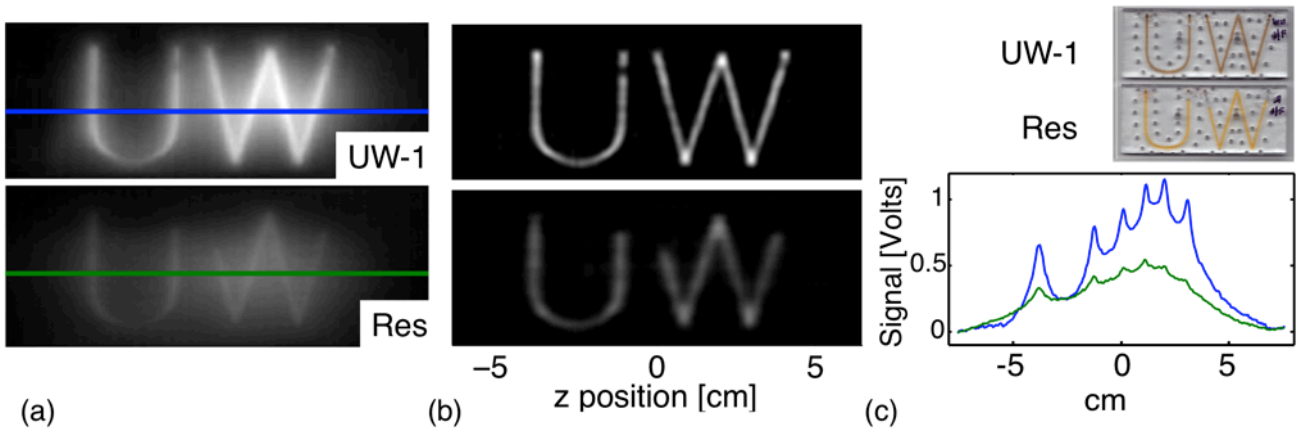

Figure 7. *x-space* phantom imaging experiments at the UC Berkeley 3D MPI scanner. (a) Native (*i.e.*, undeconvolved) MPI images of the phantoms. Channels were 1.5 mm wide and 1.5 mm deep. (b) MPI images of the phantoms, where UW-1 shows improved signal intensity and spatial resolution. Images are maximum intensity projections after mild Weiner deconvolution, with absolute intensity scaling. The imaging FOV was 4.5 x 4.5 x 14 cm^3. (c) Photograph of laser-cut acrylic phantoms containing UW-1 (top) and *Resovist*® (bottom) (top) mid-line cross-sections (bottom) of native images.

$m'(H)$) of tailored tracers under typical MPI conditions (25 kHz and 20 mT/μ_0 amplitude). Our results are consistent with simulations by Weizenecker and co-authors [42] that predicted optimized tracers would feature a slight core anisotropy with coercive fields of a few mT/μ_0.

Two distinct MPI scanners and complementary reconstruction algorithms were used to acquire and process image data during this work. However, the results obtained from the different approaches were consistent: tailored tracers resulted in similar relative improvements compared to *Resovist*® for both *system matrix* and *x-space* MPI reconstructions. Signal intensity is more easily compared between the two different approaches, given the different ways in which available spatial information is encoded; tailored tracers yielded 2-3x greater signal intensity in both approaches.

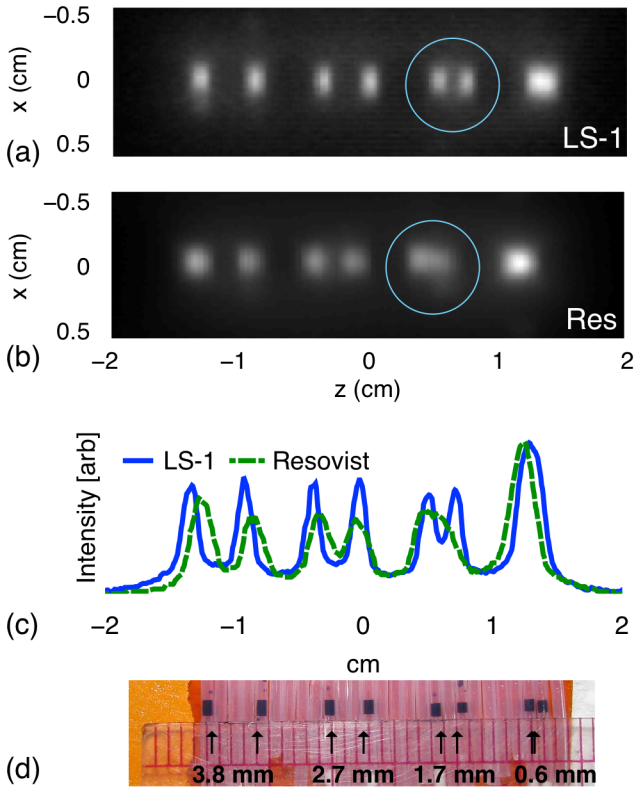

Figure 8. Resolution phantoms. Native MPI images (maximum intensity projections) of phantoms containing LS-1 (a) and Resovist (b); blue circles were overlaid for emphasis (c) cross sections. (d) photograph of the LS-1 phantom. Edge to edge separation between adjacent point sources (0.56 mm diameter) was 3.8, 2.7, 1.7, and 0.6 mm, respectively.

Better spatial resolution was demonstrated with sample LS-1 in resolution phantoms, compared with Resovist. In the LS-1 resolution phantom image, points separated by 1.7 mm were clearly resolved, in agreement with the resolution of 1.6 mm estimated from the FWHM of the PSF phantom image (not shown). We note that the FWHM resolution estimated from MPS measurements of the same tracer was 0.7 mm (calculated using 5 mT/μ_0 FWHM measured in relaxometer and 7 T/m/μ_0 gradient). The observed discrepancy between MPS and scanner resolutions is not yet fully understood. It could be caused by differences between tracer behavior in the 0D MPS system and the 3D scanner, such as alignment of the tracer nanoparticles' anisotropy axes. Some alignment is expected in the zero-dimensional MPS, but may be impeded in a scanner by multi-dimensional movement of the field-free-point.

The current results show that single-core tracers containing 26 to 27 nm (± ~1.5nm) diameter magnetic cores (as measured by TEM) provide excellent performance for MPI imaging. Recent modeling studies predicted that 25-30 nm is the optimum diameter for iron oxide MNPs, where the exact size depends on the amount of magnetocrystalline and shape anisotropy present in the tracers. [41], [42]. We attribute the improved performance of tailored tracers to their more uniform size and more optimal magnetic properties. Compared to Resovist, which has a bimodal size distribution, predominantly containing small particles ~6 nm in diameter with a small fraction of multi-core clusters with an effective 24 nm magnetic size [39], [40], samples UW-1, UW-2, and LS-1 each contained monodisperse particles with larger magnetic cores.

This article has been accepted for publication in a future issue of this journal, but has not been fully edited. Content may change prior to final publication. Citation information: DOI 10.1109/TMI.2014.2375065, IEEE Transactions on Medical Imaging

V. Conclusions

We previously determined our tailored MPI tracers were biocompatible in *in vitro* [31] and *in vivo* studies [11]. Here, we have demonstrated an approach to tracer design that yields better image quality than existing tracers, with MPI performance close to the maximum predicted by theories of nanoparticle magnetization. Tailored tracers featured a magnetic core diameter of 26 to 27 nm (± ~1.5nm) and hydrodynamic diameter of ~50 nm or ~72 nm. The new tracers displayed up to 3x greater signal intensity per unit iron than Resovist in *system matrix* and *x-space* MPI and improved spatial resolution of at least 1.7mm in native *x-space* images.

Acknowledgement

Part of this work was conducted at the University of Washington NanoTech User Facility, a member of the NSF National Nanotechnology Infrastructure Network (NNIN). We gratefully acknowledge ongoing collaborations with Prof. R. Chantrell and his group on Monte Carlo simulations.

References

[1] B. Gleich and J. Weizenecker, "Tomographic imaging using the nonlinear response of magnetic particles," *Nature*, vol. 435, no. 7046, pp. 1214–1217, Jul. 2005.

[2] P. W. Goodwill, E. U. Saritas, L. R. Croft, T. N. Kim, K. M. Krishnan, D. V. Schaffer, and S. M. Conolly, "X-Space MPI: Magnetic Nanoparticles for Safe Medical Imaging," *Advanced Materials*, vol. 24, pp. 3870–3877, 2012.

[3] K. M. Krishnan, "Biomedical Nanomagnetics: a Spin Through Possibilities in Imaging, Diagnostics, and Therapy," *IEEE Transactions on Magnetics*, vol. 46, no. 7, pp. 2523–2558, Jun. 2010.

[4] J. Weizenecker, B. Gleich, J. Rahmer, H. Dahnke, and J. Borgert, "Three-dimensional real-time in vivo magnetic particle imaging," *Phys. Med. Biol*, vol. 54, no. 5, pp. L1–L10, 2009.

[5] J. Weizenecker, J. Borgert, and B. Gleich, "A simulation study on the resolution and sensitivity of magnetic particle imaging," *Phys. Med. Biol*, vol. 52, pp. 6363–6374, 2007.

[6] R. W. Katzberg and C. Haller, "Contrast-induced nephrotoxicity: Clinical landscape," *Kidney Int*, vol. 69, pp. S3–S7, Apr. 2006.

[7] E. A. Sadowski, L. K. Bennett, M. R. Chan, A. L. Wentland, A. L. Garrett, R. W. Garrett, and A. Djamali, "Nephrogenic Systemic Fibrosis: Risk Factors and Incidence Estimation," *Radiology*, vol. 243, no. 1, pp. 148–157, Apr. 2007.

[8] "USRDS Annual Data Report Vol. 1: Atlas of Chronic Kidney Disease in the United States," Sep. 2012.

[9] M. Lu, M. H. Cohen, D. Rieves, and R. Pazdur, "FDA report: Ferumoxytol for intravenous iron

[12] C. U. Herborn, F. M. Vogt, T. C. Lauenstein, O. Dirsch, C. Corot, P. Robert, and S. G. Ruehm, "Magnetic resonance imaging of experimental atherosclerotic plaque: Comparison of two ultrasmall superparamagnetic particles of iron oxide," *J Magn Reson Imaging*, vol. 24, no. 2, pp. 388–393, 2006.

[13] J. W. M. Bulte, "In Vivo MRI Cell Tracking: Clinical Studies," *American Journal of Roentgenology*, vol. 193, no. 2, pp. 314–325, Aug. 2009.

[14] B. Zheng, T. Vazin, W. YANG, P. W. Goodwill, E. U. Saritas, L. R. Croft, D. V. Schaffer, and S. M. Conolly, "Quantitative stem cell imaging with magnetic particle imaging," *Magnetic Particle Imaging (IWMPI), 2013 International Workshop on*, p. 1, 2013.

[15] P. W. Goodwill, A. Tamrazian, L. R. Croft, C. D. Lu, E. M. Johnson, R. Pidaparthi, R. M. Ferguson, A. P. Khandhar, K. M. Krishnan, and S. M. Conolly, "Ferrohydrodynamic relaxometry for magnetic particle imaging," *Appl. Phys. Lett.*, vol. 98, no. 26, pp. 262502–262502, 2011.

[16] R. Ferguson, K. Minard, and K. Krishnan, "Optimization of nanoparticle core size for magnetic particle imaging," *J Magn Magn Mater*, vol. 321, pp. 1548–1551, 2009.

[17] P. W. Goodwill and S. M. Conolly, "The X-Space Formulation of the Magnetic Particle Imaging Process: 1-D Signal, Resolution, Bandwidth, SNR, SAR, and Magnetostimulation," *IEEE transactions on medical imaging*, vol. 29, no. 11, pp. 1851–1859, 2010.

[18] K. Lu, P. W. Goodwill, E. U. Saritas, B. Zheng, and S. M. Conolly, "Linearity and Shift Invariance for Quantitative Magnetic Particle Imaging," *IEEE transactions on medical imaging*, vol. 32, no. 9, pp. 1565–1575.

[19] R. M. Ferguson, K. R. Minard, A. P. Khandhar, and K. M. Krishnan, "Optimizing magnetite nanoparticles for mass sensitivity in magnetic particle imaging," *Med. Phys.*, vol. 38, no. 3, pp. 1619–1626, Feb. 2011.

[20] R. M. Ferguson, A. P. Khandhar, and K. M. Krishnan, "Tracer design for magnetic particle imaging (invited)," *J. Appl. Phys.*, vol. 111, no. 7, p. 07B318, 2012.

[21] J. Weizenecker, B. Gleich, and J. Borgert, "Magnetic particle imaging using a field free line," *J Phys D Appl Phys*, 2008.

[22] T. Knopp, M. Erbe, T. F. Sattel, S. Biederer, and T. M. Buzug, "Generation of a static magnetic field-free line using two Maxwell coil pairs," *Appl. Phys. Lett.*, vol. 97, no. 9, pp. 092505–092505, 2010.

[23] M. Erbe, T. Knopp, T. F. Sattel, S. Biederer, and T. M. Buzug, "Experimental generation of an arbitrarily rotated field-free line for the use in magnetic particle imaging," *Med. Phys.*, vol. 38, no. 9, p. 5200, 2011.

[24] P. W. Goodwill, J. J. Konkle, Bo Zheng, E. U. Saritas, and S. T. Conolly, "Projection X-Space

Magnetic Particle Imaging," *IEEE transactions on medical imaging*, vol. 31, no. 5, pp. 1076–1085.

[25] M. Grüttner, T. Knopp, J. Franke, M. Heidenreich, J. Rahmer, A. Halkola, C. Kaethner, J. Borgert, and T. M. Buzug, "On the formulation of the image reconstruction problem in magnetic particle imaging," *Biomed Tech (Berl)*, vol. 58, no. 6.

[26] J. Rahmer, J. Weizenecker, B. Gleich, and J. Borgert, "Signal encoding in magnetic particle imaging: properties of the system function," *BMC Medical Imaging*, vol. 9, p. 4, 2009.

[27] J. Rahmer, J. Weizenecker, B. Gleich, and J. Borgert, "Analysis of a 3-D System Function Measured for Magnetic Particle Imaging," *IEEE transactions on medical imaging*, vol. 31, no. 6, pp. 1289–1299, Jun. 2012.

[28] T. Knopp, T. Sattel, S. Biederer, J. Rahmer, J. Weizenecker, B. Gleich, J. Borgert, and T. Buzug, "Model-based reconstruction for magnetic particle imaging," *Medical Imaging, IEEE Transactions on*, vol. 29, no. 1, pp. 12–18, 2009.

[29] P. Goodwill and S. Conolly, "Multidimensional X-Space Magnetic Particle Imaging," *IEEE transactions on medical imaging*, vol. 30, no. 9, pp. 1581–1590, 2011.

[30] S. Biederer, T. Knopp, T. Sattel, Lüdtke-Buzug K, B. Gleich, J. Weizenecker, J. Borgert, and T. M. Buzug, "Magnetization response spectroscopy of superparamagnetic nanoparticles for magnetic particle imaging," *J Phys D Appl Phys*, vol. 42, p. 205007, 2009.

[31] A. P. Khandhar, R. M. Ferguson, J. A. Simon, and K. M. Krishnan, "Tailored magnetic nanoparticles for optimizing magnetic fluid hyperthermia," *Journal of Biomedical Materials Research Part A*, vol. 100, no. 3, pp. 728–737, 2012.

[32] I. Schmale, J. Rhamer, B. Gleich, J. Borgert, and J. Weizenecker, "Point Spread Function Analysis of Magnetic Particles," in *Springer Proceedings in Physics*, vol. 140, T. M. Buzug and J. Borgert, Eds. Berlin: Springer Berlin Heidelberg, 2012, pp. 287–292.

[33] B. Gleich, J. Weizenecker, H. Timminger, C. Bontus, I. Schmale, J. Rahmer, J. Schmidt, J. Kanzenbach, and J. Borgert, "Fast MPI Demonstrator with Enlarged Field of View," *Proceedings of ISMRM*, vol. 18, no. 218, Nov. 2010.

[34] J. Rahmer, B. Gleich, C. Bontus, I. Schmale, J. Schmidt, J. Kanzenbach, O. Woywode, J. Weizenecker, and J. Borgert, "Rapid 3D *in vivo* Magnetic Particle Imaging with a large field of view," *Proceedings of ISMRM*, vol. 19, no. 269, Nov. 2011.

[35] J. Rahmer, B. Gleich, J. Weizenecker, A. Halkola, C. Bontus, J. Schmidt, I. Schmale, O. Woywode, T. Buzug, and J. Borgert, "Fast continuous motion of the field of view in magnetic particle imaging," *Magnetic Particle Imaging (IWMPI), 2013 International Workshop on*, p. 1, 2013.

[36] A. Halkola, T. Buzug, J. Rahmer, and B. Gleich, "System Calibration Unit for Magnetic Particle Imaging: Focus Field Based System Function," in *Springer Proceedings in Physics*, vol. 140, T. M. Buzug and J. Borgert, Eds. Springer Berlin Heidelberg, 2012, pp. 27–31.

[37] P. Goodwill, L. R. Croft, J. Konkle, K. Lu, E. U. Saritas, B. Zheng, and S. Conolly, "Third Generation X-space MPI Mouse and Rat Scanner," in *Springer Proceedings in Physics*, vol. 140, T. M. Buzug and J. Borgert, Eds. Springer Berlin Heidelberg, 2012, pp. 261–265.

[38] P. W. Goodwill, K. Lu, B. Zheng, and S. M. Conolly, "An x-space magnetic particle imaging scanner," *Rev. Sci. Instrum.*, vol. 83, no. 3, p. 033708, 2012.

[39] D. Eberbeck, F. Wiekhorst, S. Wagner, and L. Trahms, "How the size distribution of magnetic nanoparticles determines their magnetic particle imaging performance," *Appl. Phys. Lett.*, vol. 98, no. 18, p. 182502, 2011.

[40] T. Yoshida, K. Enpuku, F. Ludwig, J. Dieckhoff, T. Wawrzik, A. Lak, and M. Schilling, "Characterization of Resovist® Nanoparticles for Magnetic Particle Imaging," in *Springer Proceedings in Physics*, vol. 140, T. M. Buzug and J. Borgert, Eds. Springer Berlin Heidelberg, 2012, pp. 3–7.

[41] R. M. Ferguson, A. P. Khandhar, H. Arami, L. Hua, O. Hovorka, and K. M. Krishnan, "Tailoring the magnetic and pharmacokinetic properties of iron oxide magnetic particle imaging tracers.," *Biomed Tech (Berl)*, vol. 58, no. 6, pp. 493–507, Dec. 2013.

[42] J. Weizenecker, B. Gleich, J. Rahmer, and J. Borgert, "Micro-magnetic simulation study on the magnetic particle imaging performance of anisotropic mono-domain particles," *Phys. Med. Biol*, vol. 57, no. 22, pp. 7317–7327, Oct. 2012.